Journal of Magnetic Resonance 199 (2009) 48–55

Contents lists available at ScienceDirect

Journal of Magnetic Resonance

journal homepage: www.elsevier.com/locate/jmr

An improved equivalent magnetization current method applied to the design of local breast gradient coils

Hector Sanchez Lopez *, Michael Poole, Stuart Crozier

The University of Queensland, School of Information Technology and Electrical Engineering, General Purpose South Building (78), Brisbane, Qld 4072, Australia

ARTICLE INFO

Article history:
Received 19 December 2008
Revised 29 March 2009
Available online 2 April 2009

Keywords:
Magnetic resonance imaging (MRI)
Equivalent magnetization current (EMC)
Gradient coil for breast imaging

ABSTRACT

Magnetic resonance imaging (MRI) is an important tool in the diagnosis of breast cancer. Increased gradient strengths and slew rates assist in terms of the potential to image with increased spatial and/or temporal resolution. Strong gradients also facilitate diffusion studies; one well-known method of increasing gradient strength is to design local gradient coils, those with reduced diameter where the gradient conductors are closer to the region of interest. In the case of breast imaging, this necessitates the use of coil geometries that lack the symmetry (e.g. cylindrical) required by some standard coil design techniques. Therefore a symmetry-free, inverse boundary element method (BEM) was employed to design a set of local breast gradient coils which would allow simultaneous imaging of both breasts. This BEM is a modified version of a previously reported equivalent magnetisation current method that now incorporates a piecewise-linear magnetisation rather than piecewise-constant. It is demonstrated that coil geometries more closely encompassing the sample shape, hence possessing wire windings located close the sample, produce superior coil performances. The use of two regions of interest instead one that covers the two samples produces superior high performance breast gradient coils. Additionally, it was demonstrated that this inverse BEM produced standard cylindrical coils with comparable properties and that the method is robust when challenged with difficult coil design problems in two other examples.

1. Introduction

High performance gradient coils are needed to meet the ever increasing demands of new techniques in magnetic resonance imaging (MRI). It is well known that making gradient coils smaller and placing their wires closer to the region of interest (ROI) increases their performance [1–4]; the efficiency, η, measured in $\mathrm{mTm^{-1}\,A^{-1}}$, of a cylindrical gradient coil is inversely proportional to the square of the radius, a, (i.e. $\eta \propto a^{-2}$). This can be achieved with local gradient coils tailored for imaging particular sub-anatomies of the human body. Local gradient coils for the head [1–4] and knee [5], for example, have been demonstrated to have increased performance over whole body gradients. It has also been recently shown that further improvements in performance of local coils may be obtained by employing a symmetry-free coil design method [6]. This ethos is exemplified in the present work by designing a set of gradient coils specifically for breast imaging, which are expected to provide improved gradient coil performance for demanding studies such as diffusion-weighted imaging of the breast [7]. Ersahin and et al. used a symmetry-free inverse boundary element method (IBEM) to design a conical gradient coil for breast imaging [8]. A target field method [9] was employed by the same group to design gradient coils for breast imaging using different geometries [10,11]. Maier et al. [12] and VanderWerf et al. [13] demonstrated the advantages of a local set of gradient coils for breast imaging, however, they were restricted to simple geometries. A different, symmetry-free method using fuzzy membership functions was used in [14] to optimize a family of curves expressed in terms of free parameters in order to produce a highly efficient gradient coil for breast imaging.

A coil design method that is free from symmetry was employed in this work to more optimally tailor the coil geometry to the target region of interest (ROI), thereby improving performance. Two separate regions were used to specify the linearity of the magnetic field produced by the gradient coils, one for each breast; it was expected that reducing the volume over which the field is specified would increase coil performance further.

Coil design methods that are independent of the shape of the current-carrying surface were pioneered in 1992 for gradient coils by Pissanetzky [15], where the current-carrying surface was discretized into a set of triangular boundary elements, each containing a uniform current density. More recently, Peeren provided a detailed mathematical description of the this approach and extended it to more general electromagnetic problems [16]. In this study an alternative approach was used which takes advantage of the equivalency between a magnetized volume and

* Corresponding author.
E-mail addresses: hsanchez@itee.uq.edu.au (H.S. Lopez), michael@itee.uq.edu.au (M. Poole), stuart@itee.uq.edu.au (S. Crozier).

1090-7807/$ - see front matter © 2009 Elsevier Inc. All rights reserved.
doi:10.1016/j.jmr.2009.03.011

a surface current density [17], that we have termed the Equivalent Magnetization Current (EMC) method [18]. The previously reported EMC method modelled the surface as piecewise-constant [18], whereas the modified method in the current paper uses a piecewise-linear magnetisation that more accurately models the surface current density. Before designing the asymmetric breast gradient coil we checked the outcomes from the EMC method by designing a set of whole-body gradients coils with the same geometry as that described by Shvartsman et al. [19] and comparing the results. Bi-planar gradient coils for open MRI systems were also designed by considering a non-ferromagnetic conducting surface to control the influence of the eddy currents in the ROI. These design examples serve to illustrate the robustness and versatility of the EMC method when designing highly constrained gradient coils.

2. Materials and methods

This section begins by describing the theory of the EMC method and how it differs from standard inverse boundary element methods (IBEM) that are based on current density. Details of the three coil design problems are then presented.

2.1. The equivalent magnetization current

The EMC model considers an isotropic, rigid, non-hysteretic, arbitrary volume, V, of thickness h, bounded by the surface S ($S \in \mathscr{R}^3$) that possesses a magnetization, $\mathbf{M}(\mathbf{r}')$, normal to S. A volume of "well-behaved" magnetization $\mathbf{M}(\mathbf{r}')$ can be considered as equivalent to a uniform current density on its surface [17]. If h is small and $\mathbf{M}(\mathbf{r}')$ is piecewise-linear throughout the thin volume, V, it can be shown that (see Eqs. (1)–(9)) in [18]

$$\mathbf{M}(\mathbf{r}')h = \psi(\mathbf{r}') \cdot \hat{\mathbf{n}}(\mathbf{r}'), \quad \mathbf{r}' \in S \tag{1}$$

where $\psi(\mathbf{r}')$ is the scalar piecewise-linear stream-function of the current density flowing on S and $\hat{\mathbf{n}}(\mathbf{r}')$ is the normal vector to S at $\mathbf{r}'$. It should be noted that an equivalent analogy can be made in which the magnetization is a unit vector normal to the surface and the thickness varies with position, $h(\mathbf{r}')$. The arbitrarily shaped surface was discretized into N_E triangular elements with N nodes. $\psi(\mathbf{r}')$, can be expressed as a sum of unknown nodal stream-function values, s_n, and basis-functions, $\psi_n(\mathbf{r}')$; $\psi(\mathbf{r}') = \sum_{n=1}^{N} s_n \hat{\psi}_n(\mathbf{r}')$ [18], which $\psi_n(\mathbf{r}')$ is linear in each triangle and therefore can be expressed as:

$$\hat{\psi}_n(\mathbf{r}') = (1 - \frac{(\mathbf{r}' - \mathbf{r}_{ni}) \cdot \mathbf{d}_{ni}}{|\mathbf{d}_{ni}|^2}) \hat{u}(\mathbf{r}'), \quad i = 1, \ldots, 0, \quad \hat{u}(\mathbf{r}') = \begin{cases} 1, & \mathbf{r}' \in \Delta_{ni} \\ 0, & \mathbf{r}' \notin \Delta_{ni} \end{cases} \tag{2}$$

where $\mathbf{d}_{ni}$ is the perpendicular distance vector from $\mathbf{r}_n$ to the far side of each triangle, Δ_{ni}, associated with the nth node (see Fig. 1) and O is the number of triangles associated with the node i. Eq. (2) ensures that $\psi_n(\mathbf{r}')$ in each triangle associated with node n has a value of one at the node n and falls linearly to zero at the edge opposite to the node n. In the rest the conducting surface ($\mathbf{r}' \notin \Delta_{ni}$)$\psi(\mathbf{r}')$ is zero. The difference between the new formulation presented in Eq. (2) and the basis function given in [18] is the intrinsic linear spatial behavior of the function $\psi(\mathbf{r}')$ and mathematically can be shown that after applying a curl operation can be obtained the basis functions presented by Pissanetzky [15] and Lemdiasov [20]. The $\psi(\mathbf{r}')$ function described in [18] assumes the value of one at the node n and zero in the rest of the triangles. This approach speeds up the calculation time however smooth wire patterns might only be generated by linear interpolation after calculation of the stream function values.

2.2. Magnetic field calculation

The flux density of magnetic field, $\mathbf{B}$, produced by a magnetized thin volume is deduced by applying the curl operator to the magnetic vector potential, $\mathbf{A}$, (Eq. (5.103), p. 197 in [17]) generated by the discontinuous finite volume, V, of magnetic dipoles;

$$\mathbf{B} = -\frac{\mu_0}{4\pi} \nabla_{\mathbf{r}} \int_V \mathbf{M}(\mathbf{r}') h \cdot \nabla_{\mathbf{r}'} \left(\frac{1}{R}\right) d\Omega' \tag{3}$$

where $R = |\mathbf{r} - \mathbf{r}'|$ is the distance between $\mathbf{r}'$, a point in the magnetized triangle, and $\mathbf{r}$, a point in the region of uniformity (ROU) where the magnetic flux density is required to exhibit a specific form and μ_0 is the permeability of free space. If we consider the piecewise-linear magnetization of V and substitute the product $\psi(\mathbf{r}') \cdot \hat{\mathbf{n}}(\mathbf{r}')$ for the magnetization-thickness function, $\mathbf{M}(\mathbf{r}')h$, Eq. (3) can be transformed to an integration over the surface area, A', and a summation over triangles and nodes of the surface. The magnetic flux density can be written as:

$$\mathbf{B}(\mathbf{r}) = -\frac{\mu_0}{4\pi} \sum_{n=1}^{N} s_n \sum_{i=1}^{O} \nabla_{\mathbf{r}} \int_{A_{ni}} \hat{\mathbf{n}}_{ni}(\mathbf{r}') \cdot \hat{\psi}_n(\mathbf{r}') \cdot \nabla_{\mathbf{r}'} \left(\frac{1}{R}\right) dA_{ni} \tag{4}$$

where O is the number of triangles associated with the node n and Ani is the area of the ith triangle belonging to node n, and the subscript ni indicates the ith triangle associated with the node n.

In MRI experiments we are usually only interested in the axial component of the magnetic flux density $B_z(x, y, z)$ due to the presence of an intense background field, $\mathbf{B} = B_0 \hat{\mathbf{z}}$. Using Eq. (4), and after some algebra, we can write:

$$B_z(x, y, z) = \sum_{n=1}^{N} s_n c_n \tag{5a}$$

where

$$c_n = -\frac{\mu_0}{4\pi} \sum_{i=1}^{O} \int_{A_{ni}} \begin{bmatrix} \frac{-3(z-z')(x-x')n_{x,ni} - 3(z-z')(y-y')n_{y,ni}}{R^5} + \cdots \\ \frac{((x-x')^2 + (y-y')^2 - 2(z-z')^2) n_{z,ni}}{R^5} \end{bmatrix} \hat{\psi}_n(\mathbf{r}') dA_{ni} \tag{5b}$$

2.3. The equivalent power, stored magnetic energy, force and torque

If a linear variation of the magnetization-thickness stream-function is assumed in the triangle then the magnetization effect can be represented by an equivalent surface current density, $\mathbf{J}$, flowing in the surface of the triangle that belongs to the node n. The same solenoidal function used in [20] to represent $\mathbf{J}$ can be used to calculate the equivalent power deduced in [6], stored magnetic energy, force and torque. Alternatively, the magnetic energy between two dipoles calculated as the work done in moving one of the dipoles from an infinite distance away to its present position can be used. The stored magnetic energy between two surface nodes, m and n, can thus be calculated by integrating over all dipoles that constitute each triangle i belonging to m and each triangle j belonging to the node n. The magnetic energy is expressed as:

$$W = \sum_{n=1}^{N} \sum_{m=1}^{N} s_n s_m L_{mn} \tag{6a}$$

where

$$L_{mn} = \frac{\mu_0}{4\pi} \sum_{i=1} \sum_{j=1} \int_{A_{mi}} \int_{A_{nj}} \frac{\hat{\mathbf{n}}_{mi} \cdot \hat{\mathbf{n}}_{nj}}{R^3} - \frac{3 \lfloor \hat{\mathbf{n}}_{mi} \cdot (\mathbf{r}_{mi} - \mathbf{r}_{nj}) \rfloor \lfloor \hat{\mathbf{n}}_{nj} \cdot (\mathbf{r}_{mi} - \mathbf{r}_{nj}) \rfloor}{R^5} \hat{\psi}_n(\mathbf{r}') \hat{\psi}_m(\mathbf{r}') dA_{mi} dA_{nj} \tag{6b}$$

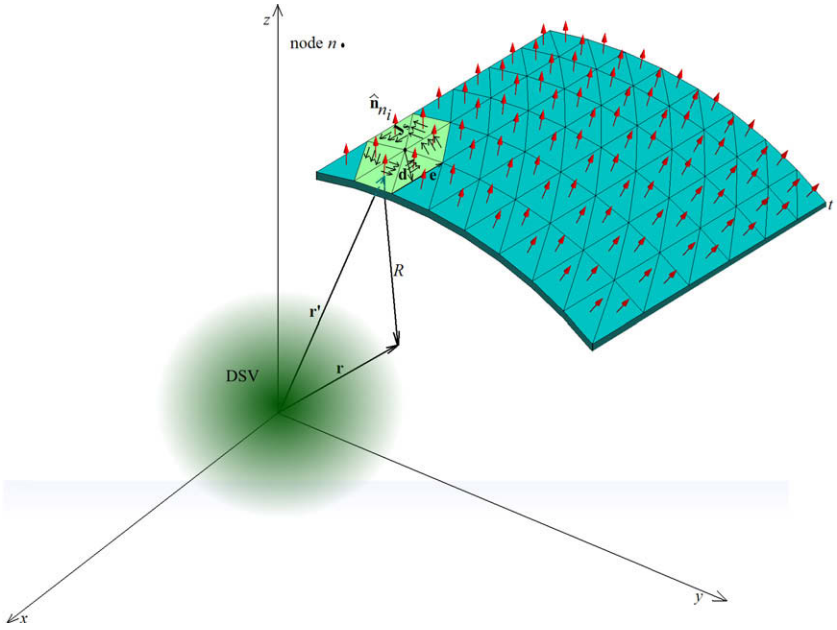

Fig. 1. Coordinates system used in this work. The source vector $\mathbf{r}'$ point at the magnetized element associated with the current node n. In light colour (green) has been highlighted the "building block" formed for O triangles associated with the node n; $i = 1 \ldots O$. The vector $\hat{\mathbf{n}}_{n_i}$ is the normal of the triangle i associated with the current node n. The vector $\mathbf{d}$ is the distance from node n to a point located in the vector $\mathbf{e}$. (For interpretation of the references to color in this figure legend, the reader is referred to the web version of this paper.)

and the vectors $\mathbf{r}_{mi}$ and $\mathbf{r}_{nj}$ are the vector positions in the triangles i and j.

2.4. Eddy current calculations

From Faraday's induction law, any change in magnetic field in time will induce current flow in a conducting domain [17], called eddy currents. These eddy currents are unwanted as they generate spurious and transient magnetic fields in the ROU. Active magnetic screening [21] can be designed by setting the magnetic flux density generated by the eddy currents in the ROU to zero. The stream-function values of the induced eddy currents, s_n^{ind}, can be explicitly calculated in terms of s_n by assuming that no resistive dissipations, no displacement currents occur and that the current in the main gradient is switched instantaneously, as presented by Peeren [16];

$$s_n^{\text{ind}} = -\mathbf{M}_{C-C}^{-1}\mathbf{M}_{C-S}s_n \tag{7}$$

where $\mathbf{M}_{C-C}$ is the self inductance matrix of the conducting surface C, $\mathbf{M}_{C-S}$ is the matrix describing the mutual inductive coupling between the gradient coil and conducting surfaces. The axial magnetic flux density arising from these eddy currents, $B_z^{\text{ind}}(\mathbf{r})$, can be also calculated using Eq. (5).The shielding effectiveness was calculated as the relative residual linear gradient G_E/G_P [22]. In this paper, we assumed that G_E is the mean residual first-order gradient in the ROU produced by the instantaneously induced eddy current and G_P is the gradient produced by the coil at the peak current. We used the ratio G_E/G_P in order to compare the shielding performance of two biplanar gradient coils.

2.5. The optimization problem

$B_z(\mathbf{r})$ and $B_z^{\text{ind}}(\mathbf{r})$ are both linear with respect to s_n, as are the torque and force generated by the coil in the intense, uniform background magnetic field, $B_0\hat{\mathbf{z}}$. The stored magnetic energy is quadratic with respect to s_n and was calculated using (6). The optimization problem is therefore stated as a quadratic programming (QP) problem in the present work:

$$\begin{aligned}
&\min \sum_{n=1}^{N}\sum_{m=1}^{N} s_n s_m L_{mn}\\
&\text{subject to}\\
&\sum_{n=1}^{N} s_n \frac{\partial c_{n,p}}{\partial x} \leqslant G_0(1+\varepsilon) \quad p = 1,\ldots,P\\
&\quad -\sum_{n=1}^{N} s_n \frac{\partial c_{n,p}}{\partial x} \leqslant -G_0(1-\varepsilon)\\
&\sum_{n=1}^{N} s_n^{\text{ind}} c_{n,p} \leqslant B_z^{\text{Shield}}\\
&\quad -\sum_{n=1}^{N} s_n^{\text{ind}} c_{n,p} \leqslant B_z^{\text{Shield}}\\
&\left|\sum_{n=1}^{N} s_n F_n^{x,y,z}\right| \leqslant F_0;\ \left|\sum_{n=1}^{N} s_n T_n^{x,y,z}\right| \leqslant T_0
\end{aligned} \tag{8}$$

where $G_0(T/m)$ is the target gradient field strength specified at P target points in the ROU, B_z^{Shield} is the maximum permissible $B_z^{\text{ind}}(\mathbf{r})$ specified on the same P points. The quantity $\frac{\partial c_{n,p}}{\partial x}$ represents the gradient of $B_z(\mathbf{r})$ with respect to position x. It is a matrix containing the contribution of each node, n, at each target point, p; if a transverse gradient in the y-direction is desired then $\frac{\partial c_{n,p}}{\partial y}$ is used; for a longitudinal gradient $\frac{\partial c_{n,p}}{\partial z}$ is employed. The parameter ε is used to relax the linearity of $B_z(\mathbf{r})$ in the ROU. Torque and force are included as inequality constraints. The parameters F_0 and T_0 are very small values to assure minimal force/torque when the coil is immerse in a homogenous magnetic field $\mathbf{B} = B_0\hat{\mathbf{z}}$. The magnetic energy was minimised in the optimisation functional. It is known that both power and stored energy minimisation often produce coils with similar performance for the same ROU and coil size [6].

The function *quadprog*, provided in MATLAB's® optimization toolbox, was employed to solve the QP problem (8). The solutions, s_n, are the stream-function values corresponding to the gradient coil with minimum inductance that satisfies the constraints placed upon the torque and force and the inequality constraints of the linearity of $B_z(\mathbf{r})$ and maximum $B_z^{\text{ind}}(\mathbf{r})$. Equally spaced contours of

$\psi(\mathbf{r}')$ were found to approximate the continuous current density by an arrangement of discrete current-carrying wires [23–25]. A contouring algorithm for generating the current pattern for discretized surface using triangular elements and uniform elemental current densities can be found in [6].

$B_z(\mathbf{r})$ was evaluated by applying the Biot–Savart law to the wire segments extracted from the contour information and the coil's efficiency, η, was determined from $B_z(\mathbf{r})$. The inductance and resistance of each coil was evaluated and validated using the software FastHenry [26]. FastHenry is a multipole-accelerated impedance extraction program that accepts the wires positions and their thicknesses and models the inductance and resistance of the coil. Although FastHenry was used to validate our theoretical values for the inductance and resistance, it is expected that differences between these two theoretical methods and the measured impedance of a real coil would be evident, as is often the case when predicting DC or low frequency impedances by simulation.

2.6. Gradient coil design problems

Before embarking on the breast gradient coil design, we aim to validate the EMC method by designing a conventional whole-body gradient set based on the dimensions specified in [19]; the two designs were then compared to ensure the EMC method produced comparable results. A simplified model of a biplanar gradient coil was designed in order to demonstrate the robustness of the EMC method when applied to highly constrained, complex geometries and the effect of the eddy currents was controlled in the ROU. The design of novel asymmetric gradient coils for breast imaging was then performed. The triangular boundary element meshes used to design all the coils were generated using GMSH [27]. GMSH is an automatic 3D finite element grid generator with a built-in CAD engine and post-processor. It provides a simple meshing tool for academic problems with parametric input and advanced visualization capabilities.

Fig. 2(a) shows half of the geometry of the triangular discretization of the surface for the whole-body gradient coil where dimensions are the same as those presented by Shvartsman et al. [19]. In addition to that which is shown in Fig. 2, a 1.6-m long cylindrical surface with 0.475 m radius was assumed to be the eddy current surface in the whole-body gradient coil (a) and in the breast gradient coil (c).

Continuous current density and discrete wire coil design methods have previously been used for circular and rectangular biplanar gradient coils for open magnets [28–30]. However, when applying these methods to shielded coils in a very limited space, e.g. 42 cm and 50 cm primary and secondary coil radii, large numbers of turns are generally observed at their periphery. In the coils designed in the present work, a conical surface, as presented by [18,31,32] for open gradients and applied to cylindrical gradients by [33,34], is provided that joins the primary and secondary coils, thereby allowing the return paths for the wires of primary coil and the wires that provide magnetic shielding to be one and the same. Fig. 2(b), shows the surface geometry and ROU used in this example. The primary and secondary coil radii were set to 42 cm and 50 cm and were located at $Z = \pm 23$ cm and $Z = \pm 29$ cm, respectively. This design differs from those presented in [18] in the way that the shielding conditions are specified. In [18] a weak shielding condition was imposed by a set of target points specified at a virtual conducting surface while in the present work the magnetic field produced by the induced eddy currents was controlled at the ROU. The same target points used to specify the target field are employed to constrain the eddy current induced magnetic field to below 1 μT. The pole faces of a permanent magnet were included as the eddy current conducting surfaces surrounding the biplanar coil. A non-ferromagnetic and conducting pole face is assumed in order to simplify the

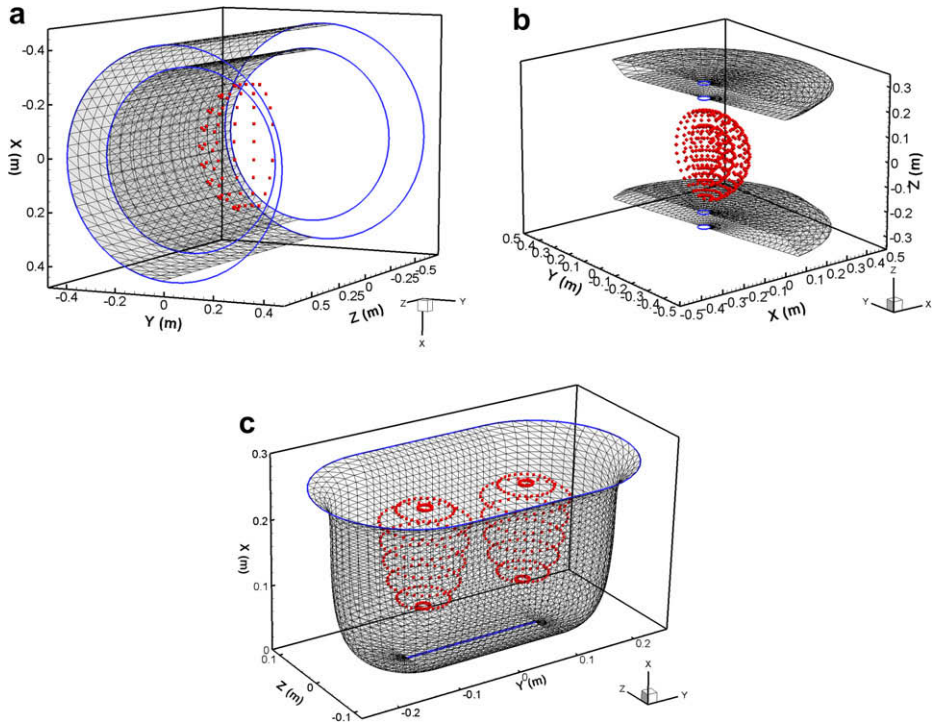

Fig. 2. Geometry of the (a) whole body and (b) biplanar gradient coil. Only half of the coil structure and DSV target points (red dots) are shown. The structure of the breast gradient coil (c). Target points are specified on the surface of two DSV (c) (red dots). Blue line represents the nodes located at the coil boundaries. Values might be assigned to the nodes at the coil boundaries. The mesh was generated using GMSH [27]. (For interpretation of the references to color in this figure legend, the reader is referred to the web version of this paper.)

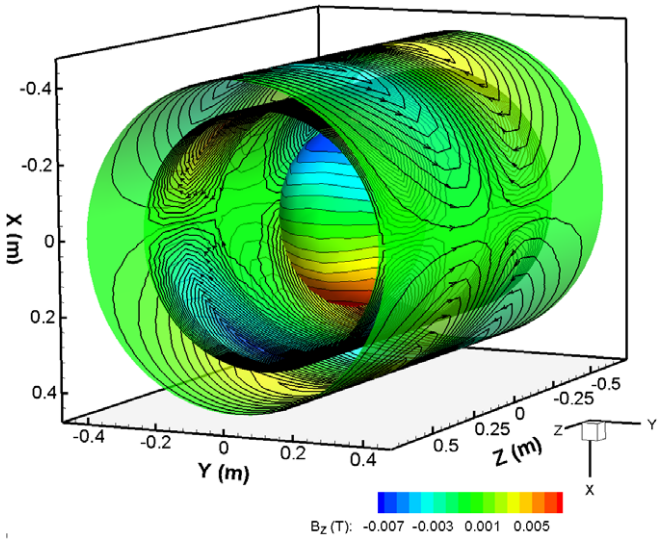

Fig. 3. Whole-body transverse gradient coil designed using the EMC method. A gap of 1 mm between wires was assumed. The arrow in the coil pattern represents the sense of the current. Contour line at the DSV represents the values of the axial magnetic field component (units in Tesla) for an operating current of 405.95 (A).

design. Because of its irregular shape the pole face lies between 1 cm and 4 cm from the secondary coil surface. In this example we have employed the same coil dimension used in [35].

Quadrupolar and fingerprint coils have previously been designed as gradient coils for breast imaging [12–14]. Fig. 2(c) shows the geometry of the current-carrying surface and ROUs for the breast imaging gradient coils. We employed similar coil dimensions used in [14], but we have extended the geometry along the *y*-direction and designed an asymmetric current-carrying surface to more closely encompass the breasts; two ROUs that mimic the breast shape have been used. Each ROU has the same dimension used in [12] but shifted along the *y*-direction. The coil surface is discretized in 5440 triangles and 2800 nodes; 464 target points were set on the surface of the two targets ROUs.

Table 1
Characteristics of the whole-body *x*-gradient coils designed using EMC and *z*-intercepts [19] methods.

Properties	EMC (this work)	*z*-Intercepts [19]
Coil radius (P/S) (mm)	344/435	344/435
Number of turn per quadrant (P/S)	23/11	23/11
Total electric length (mm)	1074.4/1356	1074.4/1356
Conductor thickness (mm) (P/S)	4.9/1.8	4.9/1.8
Conductor constant width (mm) (P/S)	6.4/17.8	5.75/17.8
Gap between wires (mm)	1	
Efficiency η (μT/m/A)	75.6	73.9
Coil inductance (μH)	662.6 (679.8)[a]	653.3
FoM, η^2/L ($T^2 \cdot m^{-2} \cdot A^{-2} \cdot H^{-1}$)	$0.0861 \cdot 10^{-4}$	$0.0836 \cdot 10^{-4}$
Coil resistance (mΩ)	138 (133.6)[a]	119
Nonuniformity (%) at $z = 0.2$ m, $x = y = 0$	−23.5	−24.6
Nonlinearity (%)at $x = 0.25$ m, $y = z = 0$	1.35	3.4
Slew rate (mT/m/ms) at $G_0 = 30$ mT/m and 1200 V	130.4 Current = 405.95 (A)	130.3

[a] Bracketed values of inductance and resistance were calculated using FastHenry [26].

3. Results and discussions

For comparison, a FoM, given by η^2/L, was used to characterise coil performance [36]. Non-linearities and non-uniformities of the magnetic flux density gradient were calculated using Eqs. (24–27)

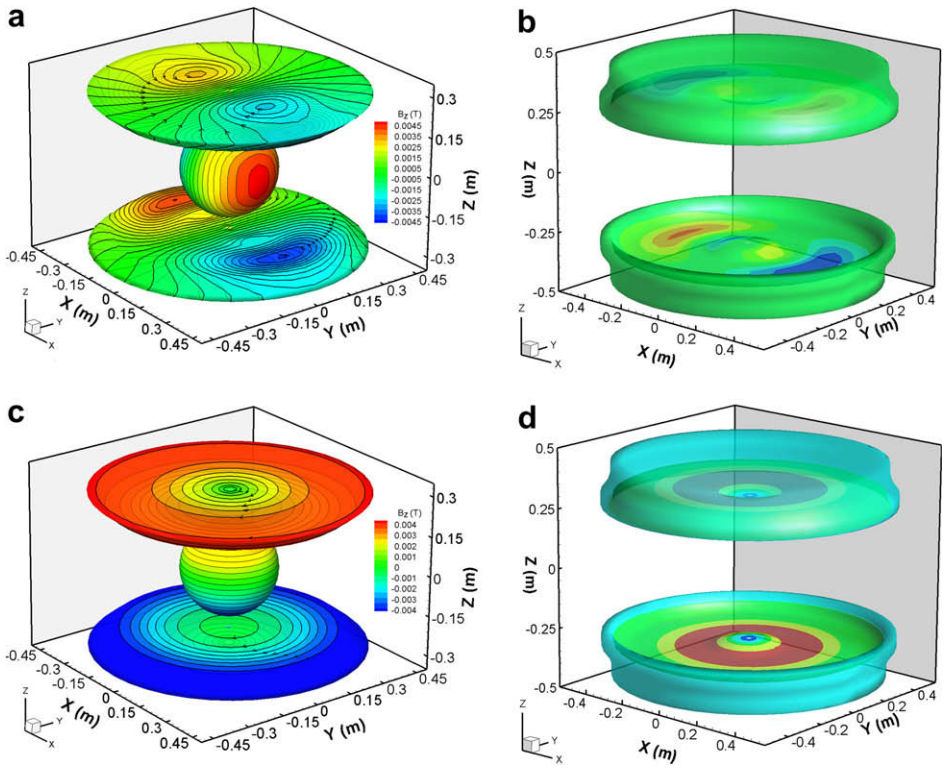

Fig. 4. Three-dimensional transverse biplanar (a) and longitudinal (c) gradient coil designs. Contour line in the DSV indicates the magnetic field axial component variation (units in Tesla) with the coordinates for an operating current of 482 (A). The arrow in the coil pattern indicates the current sense (c). Stream function contours of the Eddy current induced by the transverse (b) and longitudinal (d) gradient coils. The colour scale (colour version) in (b) and (d) are given in arbitrary units.

in [37]. The maximal deviation from the target flux density in the ROU was calculated using Eq. (6) in [6]. In Example 2, the shielding effectiveness is measured as ratio G_E/G_P [22] for the instantaneously induced eddy currents.

3.1. Example 1: whole body symmetric transverse gradient coil

Approximately 62 min was taken by a Dual Core Pentium Laptop @ 2.00 GHz to perform the coil calculation. Fig. 3 shows the wire pattern of the transverse whole body gradient coil design obtained applying this work. Table 1, summarise the performance characteristics of two coils designed using EMC and the *z*-intercepts [19] methods. The coil designed with EMC exhibited similar performance in comparison with the *z*-intercept coil; only a slightly improvement was obtained in the magnetic field spatial quality. The conductor constant width was 6.4 mm wider in the EMC coil assuming 1 mm gap between conductors. The inductance and the resistance values calculated using FastHenry [26] software is shown in parenthesis. The values predicted with EMC method were similar to the predicted by FastHenry [26] software.

In this case, the eddy current surface was 4 cm away in the radial direction from the outermost coil surface and if a shielding condition were to have been specified by constraining the magnetic field to be zero at the eddy current surface, a solution with highly oscillatory current pattern and low performance would have been obtained.

3.2. Example 2: whole body biplanar gradient coils for open magnets

Fig. 4(a and c) shows the transverse and longitudinal gradient coil patterns obtained with the EMC method. Smooth coil patterns were obtained despite the relative closeness of the outermost surface to the conducting eddy current domain. Fig. 4(b and d) shows the simulated instantaneous eddy currents induced on the pole faces. Table 2, summarises the characteristics of the actively shielded gradient coils designed using the present approach. The second column shows the properties of a partially shielded biplanar coil obtained using the approach presented in [18]. We realize that both biplanar transverse gradient coils present similar FoM; however the shielding efficiency was 3.42 times larger than the ones produced by the partially shielded design [18]. This result was due to the extra degree of freedom introduced by the control

Table 2
Characteristics of the biplanar *x*- and *z*-gradient coil designs.

Properties	Transverse (this work)	Transverse [18]	Longitudinal (this work)
Coil radius (P/S) (mm)	420/500	420/500	420/500
Number of turns per half	36	32	20
Coil half separation (P/S) (mm)	230/290	230/290	230/290
Conductor thickness (mm)	3	3	3
Conductor constant width (mm)	3	3	3
Gap between wires (mm)	1		
Efficiency η (μT/m/A)	56.1	62.22	52.1
Coil inductance (μH)	230.5 (239.3)[a]	299.31 (307.24)[a]	71.22 (75.4)[a]
FoM, η^2/L ($T^2 \cdot m^{-2} \cdot A^{-2} \cdot H^{-1}$)	$0.136 \cdot 10^{-4}$	$0.129 \cdot 10^{-4}$	$0.38 \cdot 10^{-4}$
Coil resistance (mΩ)	223 (220)[a]	(220)[a]	102.1 (98.9)[a]
Max. field error, ΔB_z^{max} (%)	3.5	5	5
G_E/G_P (%)	4.44	15.17	0.21

[a] Bracketed values of inductance and resistance were calculated using FastHenry [26].

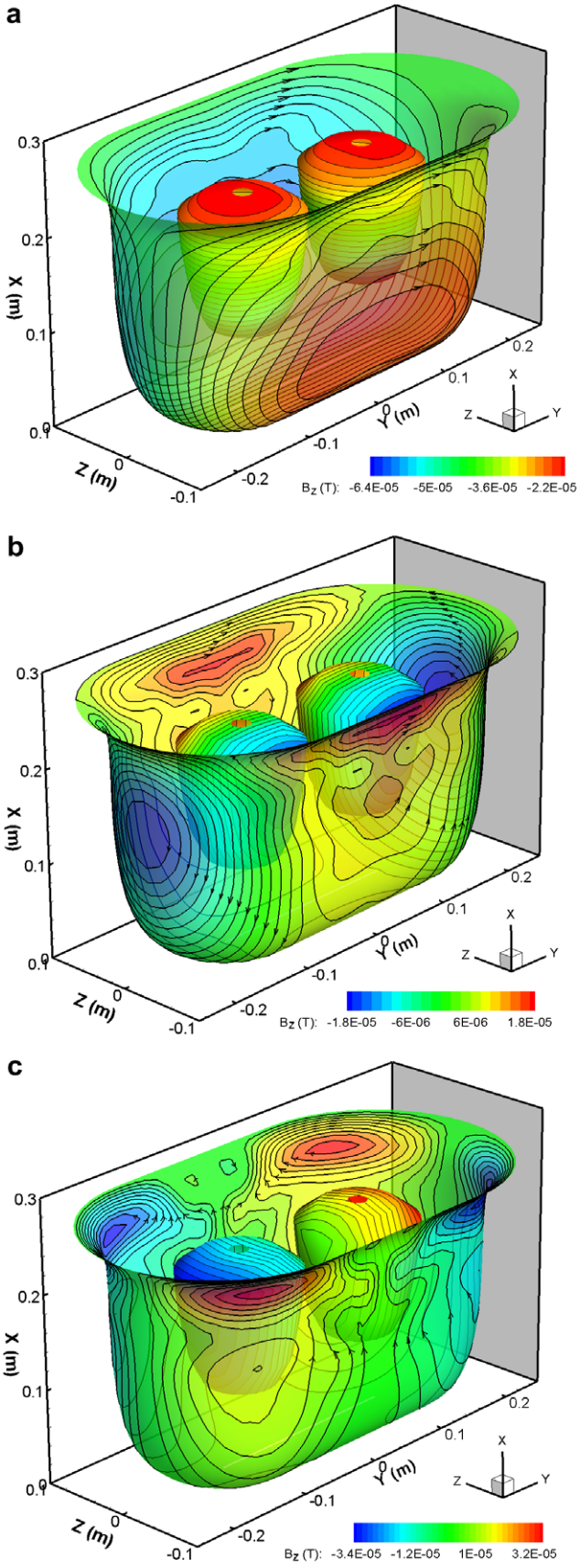

Fig. 5. (a)*x*- (b) *z*- (c) *y*-gradient coils for breast imaging. Contour line in the DSV indicates the magnetic field axial component variation (units in Tesla) with the coordinates for an operating current of 1 (A). The arrow in the coil pattern represents the sense of the current.

of the eddy current at the ROU instead of specifying stringent constraints on magnetic field values at the conducting surface. The longitudinal gradient coil showed a superior FoM and shielding performance than the transverse gradient coils.

These design examples illustrate the robustness and the versatility of the EMC method to be applied to highly asymmetric gradient coil design.

3.3. Example 3: gradient coil designs for breast imaging

Fig. 5(a–c) shows the current pattern of the *x*-, *y*- and *z*-gradient coils. Table 3, summarises the performance characteristics of the three coils designed using this EMC. If we compare the FoM of the coil Fig. 5(a) with the performance of the modified fingerprint coil presented in [14] we realize that the modified coil [14] has 1.6 times greater FoM than the design presented in this work which is due to the surface being smaller. However, the new proposed structure (see Fig. 2(c)) would permit imaging of both breasts simultaneously. If one large ROU is used instead of two smaller ones, the coil FoM decreases by as much as 0.7 times, the resistance increases dramatically and the gap between wires is reduced from 1 mm to 0.0001 mm producing a complex and impractical design. In the three-gradient coils the factor G_E/G_P were smaller in comparison with a typical shielded whole-body gradient coil (between 2.5 and 5 times smaller [34]). The coil current pattern shown in Figs. 5(a–c) produces almost zero torque where the larger torque is produced in the *z*-gradient coil along the *y*-direction and is a result of the approximation of the continuous current density by discrete wires, but is still very small. In the torque/force calculations we assumed a homogenous magnetic field, for an accurate evaluation of this parameter however the background spatial magnetic field values are required.

Comparing the FoM generated by the dedicated *x*-gradient coil (Table 3) and the same value produced by the whole-body coil showed in Table 1, the FoM produced by the dedicated coil appears, unsurprisingly, to be about 130 times larger than the same value generated by the whole-body coil due to its greatly reduced size. However, peripheral nerve stimulation (PNS) is known to be a physiological barrier to increased gradient slew-rates. Comparing the likelihood of PNS occurring with these coils is beyond the scope of this work, but some idea about that likelihood may be extrapolated from the peak magnetic field. The peak magnetic field produced by the whole-body gradient coil is approximately 13% higher than the breast coil for a given slew-rate and gradient strength, but the peak field would occur at different positions on the subject and therefore it is impossible to conclude which coil is most likely to induce PNS without subjective trials, but it is an important issue that must be addressed before building coils whose wires are so close to the body.

Table 3
Characteristics of the *x*-, *y*- and *z*-gradient coil designs from breast imaging.

Properties	*x*-Gradient	*z*-Gradient	*y*-Gradient
Max. aperture in *z*,*y* (mm)	280, 500		
Depth in *x* (mm)	260		
DSV-*x*–*y*–*z* (mm)	140.5–120–120.8		
Wire diameter (mm)	6.6	2.72	1.7
Gap between wires (mm)	1		
Number of contour lines	22	22	22
Efficiency η (μT/m/A)	313.7	291.6	238.86
Coil Inductance (μH)	88.54	81.04 (82.8)[a]	63.1
FoM, η^2/L ($T^2{\cdot}m^{-2}{\cdot}A^{-2}{\cdot}H^{-1}$)	$11.113 \cdot 10^{-4}$	$10.5 \cdot 10^{-4}$	$9.04 \cdot 10^{-4}$
Coil Resistance (mΩ)	11.27	83.15 (83.2)[a]	190.8
Max. field error, ΔB_z^{max}] (%)	4.13	4.44	4.46
Torque *x*,*y*,*z* (N·m/A·T)	0, $1.2 \cdot 10^{-3}$, 0	0,$11.2 \cdot 10^{-3}$, 0	$0.12 \cdot 10^{-3}$, $2 \cdot 10^{-3}$, 0
$\|\mathbf{B}\|_{max\ DSV}$ (mT; Current = 1 A)	0.067	0.055	0.061

[a] Bracketed values of inductance and resistance were calculated using FastHenry [26].

4. Conclusions

New gradient coils for breast imaging have been designed using the EMC method. The novel geometry allows simultaneous imaging of both breasts yet displays similar performance to other local coils previously presented. This was largely due to the ability of the symmetry-free coil design method to optimally tailor the shape of the coil to match that of the imaging region. The uses of two ROU instead one large ROU simplify the coil current pattern and hence superior coil performance is obtained. These gradients may be useful in the quest to detect and diagnose the small cancerous legions indicative of early-stage breast cancer by enabling high spatio-temporal imaging, for example.

Whole-body gradient coils were designed using the EMC method that exhibited similar performance to a reference coil of identical geometry [19] thereby indicating that practical designs can be generated using the EMC method. In addition, biplanar gradient coils for open system were designed to illustrate the robustness of the EMC method when it is used to solve problems of highly restricted geometry and magnetic field constraints. An advantage of the EMC method is the ability to include eddy currents in the design process.

Acknowledgment

This work was supported by the Australian Research Council.

References

[1] A.M. Abduljalil, A.H. Aletras, P.-M.L. Robitaille, Torque free asymmetric gradient coils for echo planar imaging, Magn. Reson. Med. 31 (1994) 450–453.
[2] D.C. Alsop, T.J. Connick, Optimization of torque-balanced asymmetric head gradient coils, Magn. Reson. Med. 35 (1996) 875–886.
[3] B.A. Chronik, A. Alejski, B.K. Rutt, Design and fabrication of a three-axis edge ROU head and neck gradient coil, Magn. Reson. Med. 44 (2000) 955–963.
[4] S. Crozier, K. Luescher, G. Hinds, W.U. Roffmann, D.M. Doddrell, Designs for an asymmetric gradient set and a compact superconducting magnet for neural magnetic resonance imaging, Rev. Sci. Instrum. 70 (1999) 4062–4066.
[5] S. Crozier, W.U. Roffmann, K. Luescher, C. Snape-Jenkinson, L.K. Forbes, D.M. Doddrell, An openable, high-strength gradient set for orthopedic MRI, J. Magn. Reson. 139 (1999) 81–89.
[6] M. Poole, R. Bowtell, Novel gradient coils designed using a boundary element method, Concept Magn. Reson. B 31B (2007) 162–175.
[7] S. Sinha, U. Sinha, Functional magnetic resonance of human breast tumors: diffusion and perfusion imaging, Ann. N.Y. Acad. Sci. 980 (2002) 95–115.
[8] A. Ersahin, H.K. Lee, O. Nalcioglu, Asymmetric gradient coil design for high resolution breast imaging, in: Proceedings of the International Society for Magnetic Resonance in Medicine, 1995, p. 954.
[9] R. Turner, Gradient coil design: a review of methods, Magn. Reson. Image 11 (1993) 903–920.
[10] H.K. Lee, A. Ersahin, O. Nalcioglu, A bilateral cylindrical gradient coil for microscopic breast imaging, in: Proceedings of the International Society for Magnetic Resonance in Medicine, 1995, p. 953.
[11] H.K. Lee, R. Raman, R. Slates, A. Ersahin, O. Nalcioglu, An optimized gradient coil for breast imaging, in: Proceedings of the International Society for Magnetic Resonance in Medicine, 1995.
[12] C.F. Maier, H.N. Nikolov, K.C. Chu, B.A. Chronik, B.K. Rutt, Practical design of a high-strength breast gradient coil, Magn. Reson. Med. 39 (1998) 392–401.
[13] K.L. VanderWerf, J.T.D. Bever, K.B. Pauly, B.A. Chronik, Design and fabrication of a three-axis hybrid-quadrupole gradient coil for MR of the Breast, in: 14th Annual Meeting of ISMRM, Seattle, USA, 2006, p. 1368.
[14] H. Sanchez, F. Liu, A. Trakic, E. Weber, S. Crozier, Three-dimensional gradient coil structures for magnetic resonance imaging designed using fuzzy membership functions, IEEE Trans. Magn. 43 (2007) 3558–3566.
[15] S. Pissanetzky, Minimum energy MRI gradient coils of the general geometry, Meas. Sci. Technol. 3 (1992) 667–673.
[16] G.N. Peeren, Stream function approach for determining optimal surface currents, J. Comput. Phys. 191 (2003) 305–321.
[17] J.D. Jackson, Classical Electrodynamics, Wiley, New York, 1998.

[18] Hector Sanchez Lopez, Feng Liu, Michael Poole, S. Crozier, The equivalent magnetization current method applied to the design of gradient coils for MRI, IEEE Trans. Magn. 45 (2009) 1–9.
[19] Shmaryu Shvartsman, M.C. Steckner, Discrete design method of transverse gradient coils for MRI, Concept Magn. Reson. B 31B (2007) 95–115.
[20] R.A. Lemdiasov, R. Ludwig, A stream function method for gradient coil design, Concept Magn. Reson. B 54 (2005) 656–668.
[21] R. Bowtell, P. Mansfield, Gradient coil design using active magnetic screening, Magn. Reson. Med. 17 (1991) 15–21.
[22] P. Blumler, B. Bliimich, R. Botto, E. Fukushima, Spatially Resolve Magnetic Resonance, WILEY-VCH, Verlag GmbH, 1998.
[23] J.F. Schenck, M.A. Hussein, W.A. Edelstein, Transverse gradient field coils for nuclear magnetic resonance imaging, USA, 1983.
[24] W.A. Edelstein, J.F. Schenck, Current streamline method for coil construction, USA, 1987.
[25] M.A. Brideson, L.K. Forbes, S. Crozier, Determining complicated winding patterns for shim coils using stream functions and the target-field method, Concept Magn. Reson. 14 (2002) 9–18.
[26] M. Kamon, M. Tsuk, J. White, FastHenry: a multipole-accelerated 3-D inductance extraction program, IEEE Trans. MTT 42 (1994) 1750–1758.
[27] C. Geuzaine, J.-F. Remacle, Gmsh reference manual: the documentation for Gmsh, a finite element mesh generator with built-in pre-and post-processing facilities, 2008. Available from: <http://www.geuz.org/gmsh/>.
[28] K. Yoda, Analytical design method of self-shielded planar coils, J. Comput. Phys. 67 (1990) 4349–4353.
[29] M.A. Martens, L.S. Petropoulos, R.W. Brown, J.H. Andrews, M.A. Morich, J.L. Patrick, Insertable biplanar gradient coils for magnetic resonance imaging, Rev. Sci. Instrum. 62 (1991) 2639–2645.
[30] L. Forbes, S. Crozier, Novel target-field method for designing shielded biplanar shim and gradient coils, IEEE Trans. Magn. 40 (2004) 1929–1938.
[31] J.F. Schenck, Transverse gradient coil, 5 561 371, US Patent, 1996.
[32] M. Abe, Y. Imamura, T. Yatsuo, Gradient coil and magnetic resonance imaging apparatus using the same, USA. 2008.
[33] R. Kimmlingen, M. Gebhardt, J. Schuster, M. Brand, F. Schmitt, A. Haase, Gradient system providing continuously variable field characteristics, Magn. Reson. Med. 47 (2002) 800–808.
[34] S.H. Shvartsman, M. Morich, G. Demeester, Z. Zhai, Ultrashort shielded gradient coil design with 3D geometry, Concept Magn. Reson. 26B (2005) 1–5.
[35] Wentao Liu, D. Zu, X. Tang, H. Guo, Target-field method for MRI biplanar gradient coil design, J. Phys. D: Appl. Phys. 40 (2007) 4418–4424.
[36] J.W. Carlson, K.A. Derby, K.C. Haveryszko, M. Weideman, Design and evaluation of shielded gradient coils, Magn. Reson. Med. 26 (1992) 191–206.
[37] S.M. Shvartsman, R.W. Brown, Y.C. Cheng, T.P. Eagan, H. Fujita, M.A. Morich, L.S. Petropoulos, J.D. Willig, Application of the SUSHI method to the design of gradient coils, Magn. Reson. Med. 45 (2001) 147–155.